25 Jul 2023

In-situ Lock-in Thermographic Measurement Of Powder Layer Thermal Diffusivity And Thickness In Laser Powder Bed Fusion

Tao Liu

Edward C. Kinzel

Ming-Chuan Leu
Missouri University of Science and Technology, mleu@mst.edu

Recommended Citation

T. Liu et al., "In-situ Lock-in Thermographic Measurement Of Powder Layer Thermal Diffusivity And Thickness In Laser Powder Bed Fusion," *Additive Manufacturing*, vol. 74, article no. 103726, Elsevier, Jul 2023.
The definitive version is available at https://doi.org/10.1016/j.addma.2023.103726

Additive Manufacturing 74 (2023) 103726

Contents lists available at ScienceDirect

Additive Manufacturing

journal homepage: www.elsevier.com/locate/addma

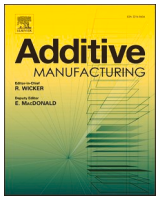

In-situ lock-in thermographic measurement of powder layer thermal diffusivity and thickness in laser powder bed fusion

Tao Liu [a,*], Edward C. Kinzel [b], Ming C. Leu [a]

[a] Mechanical and Aerospace Engineering Department, Missouri University of Science and Technology, Rolla, MO 65409, USA
[b] Aerospace and Mechanical Engineering Department, University of Notre Dame, Notre Dame, IN 46556, USA

ARTICLE INFO

Keywords:
Thermal wave
Lock in thermography
Laser powder bed fusion
Thermal diffusivity
Powder layer thickness

ABSTRACT

The thermal transport properties of the powder layer play a crucial role in the process of laser powder bed fusion (LPBF). This paper introduces an in-situ measurement method utilizing active lock-in infrared thermography (LIT) to determine the thermal diffusivity and thickness of the powder layer. The proposed method exhibits great potential for accurate powder property and thickness measurements and real-time process monitoring. In this lock-in thermographic technique, the LPBF laser beam is directed through an optical diffuser and modulated into a square thermal wave. This thermal wave serves as an active heat source to heat the surface of the powder bed. The surface temperature response is captured using a long-wave infrared (LWIR) camera. A one-dimensional thermal model is employed to provide insights into heat transfer in the frequency domain. The frequency-dependent phase response of temperature is influenced by the effective thermal diffusivity and thickness of the powder layer. This model is validated experimentally first and then utilized to measure the thermal diffusivity of different powder layers created using various particle sizes and wiper spreading speeds. Larger particle size and slower wiper spreading speed are shown to produce higher thermal diffusivity. Finally, the paper shows how this technique can be used to measure the powder layer thickness over printed geometries. This capability enables the detection of deviations in the fused part surface or errors in the wiper through analysis of resulting variations in the powder. These findings highlight the potential of the lock-in thermographic technique for rapid in-situ inspection of the new powder layer in laser powder bed fusion (LPBF) processes.

1. Introduction

Laser powder bed fusion (LPBF) is an additive manufacturing (AM) technique known for its high precision and ability to fabricate complex metallic parts [1]. The thermal properties of the powder used in LPBF significantly influence the heat transfer rates during the process [2,3], ultimately affecting the resulting part's microstructure and mechanical properties [4,5].

Metal powders, compared to their solid counterparts, exhibit lower thermal diffusivity [6,7]. In LPBF, this lower thermal diffusivity of the powder surrounding the melt pool leads to slower heat dissipation [8], resulting in a prolonged melt state and deeper melt pool depth into the powder layer [9–11]. The thermal gradient [12], solid-liquid interface velocity [13], and solidification rate [14] are all influenced by the powder's thermal diffusivity [15]. In addition, powder's lower thermal diffusivity contributes to local overheating for overhangs, cavities, and fine feature structures, impacting the solidification process [16–19] by introducing defects such as microstructure heterogeneity [20], residual stress variations [21], surface roughness [22], and porosity [23].

Studies have shown that local powder thermal diffusivity is not constant and can vary with different process parameters [24]. For instance, the spreading speed of the wiper affects powder bed packing density [25,26], leading to variations in thermal diffusivity [27]. Faster spreading speeds result in poorer powder bed quality such as higher void fraction, and lower packing density [28], increasing the risk of laser penetration [29] and keyhole defect formation [30,31]. Conversely, lower spreading speeds have been observed to improve packing density [32], surface roughness [33], and fusion zone symmetry [34]. Particle size [35], varying cohesiveness [36], flowability [37], packing fraction [38] and laser absorptivity [39,40], also influences powder thermal diffusivity [41], affecting the mechanical properties [42], surface quality [43,44], and porosity of the final part [45–47]. Additionally, the choice of process gas, particularly helium [48,49], can impact powder thermal diffusivity due to its higher thermal diffusivity compared to

* Corresponding author.
E-mail address: tlkv5@umsystem.edu (T. Liu).

https://doi.org/10.1016/j.addma.2023.103726
Received 16 June 2023; Received in revised form 3 August 2023; Accepted 3 August 2023
Available online 5 August 2023

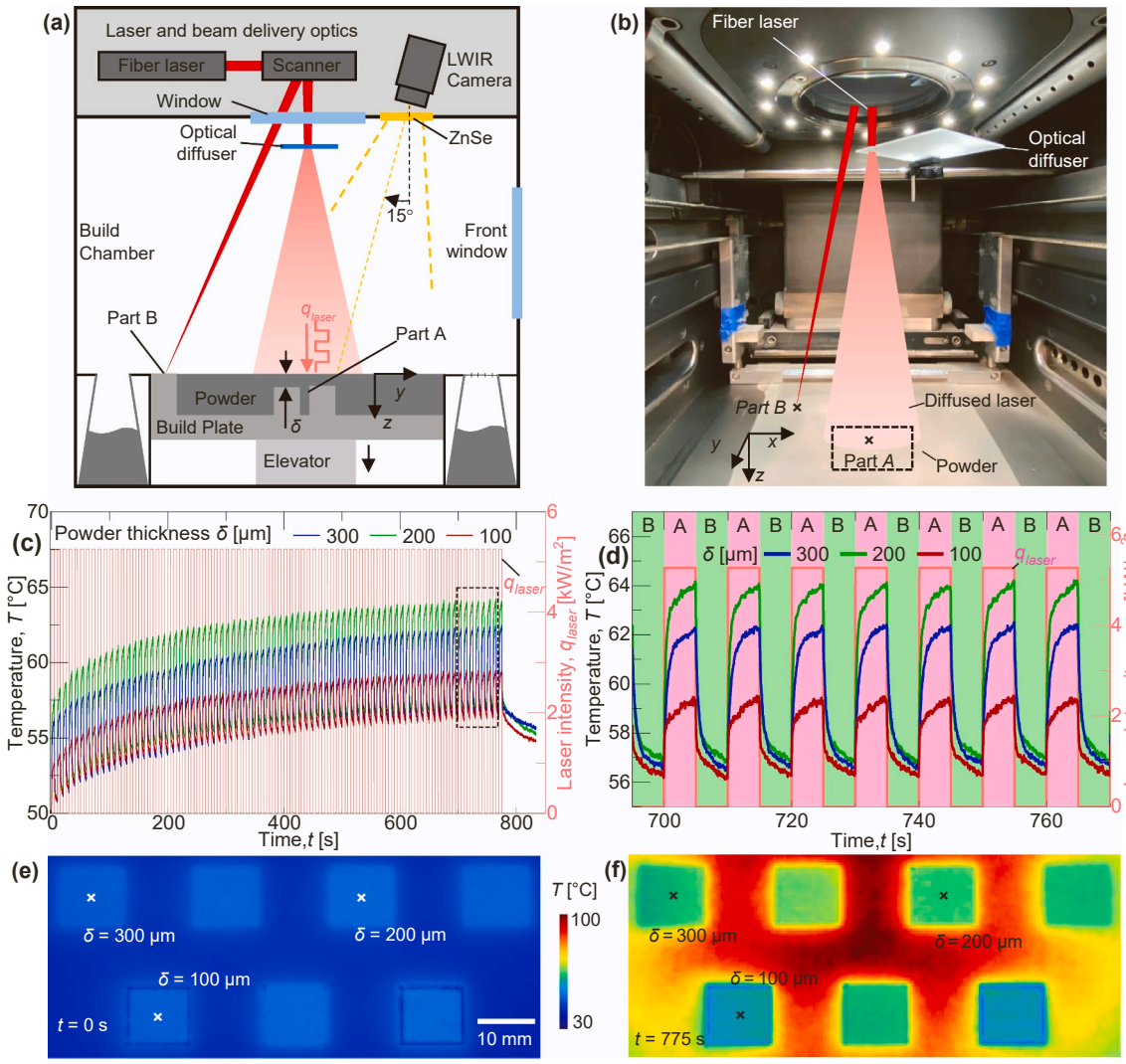

Fig. 1. (a) Schematic of the square thermal wave setup within an LPBF system, including an LWIR camera and an optical diffuser. (b) Photograph of the testing setup. (c) LWIR camera-recorded temperature history for selected points with varying powder thicknesses and (d) the last seven cycles. Note that the absolute amplitude of the $\delta = 200$ μm powder layer is highest because of the non-uniform illumination. (e) Frame of LWIR camera images at $t = 0$ s and (f) $t = 775$ s.

argon and nitrogen [50,51].

Various techniques exist for measuring powder thermal diffusivity, including the transient hot-wire method [17], transient plane source method [52], laser flash method [7,53,54], and Ångström's method [55]. However, these ex-situ measurements pose challenges in LPBF to effectively account for gas infiltration, wiper spreading, powder distribution, and printing process variability since they are difficult to perform in-situ in an LPBF machine. Alternatively, infrared thermography, a non-destructive testing technique [56,57] offering real-time [58–60], contactless [61,62], and wide-area measurements [63], shows potential for in-situ measurement of powder layer thermal diffusivity in LPBF.

This paper investigates the application of an active infrared thermography technique known as thermal wave imaging or lock-in thermography [64–66] in LPBF. By diffusing the LPBF laser through an optical diffuser and modulating it as a periodic square thermal wave heat source, the powder bed surface is actively illuminated. The surface thermal temperature response is captured using a long-wave infrared (LWIR) camera, and the extracted phase difference from the temperature history enables the determination of the powder layer's thermal diffusivity and thickness. The utilization of the LPBF laser as the heat source eliminates the need for an additional heat source. The square thermal wave input allows for the simultaneous collection of multiple frequencies within the same experiment [67]. The lock-in thermographic method exhibits higher accuracy compared to the laser flashing method by effectively filtering out noise from other frequencies [68]. Additionally, the in-situ approach employed in this study maintains the printing environment conditions, which has not been experimentally demonstrated in previous ex-situ powder thermal diffusivity measurements [69].

This in-situ method enables real-time monitoring of product areal surface topography and distortion by capturing variations in powder layer thickness, thus facilitating quality assurance and process control. It also accelerates rapid process development through the utilization of thermal properties and surface topography to optimize laser and printing parameters, achieving the desired temperature distribution and solidification characteristics [70]. Furthermore, the integration of thermal wave with large-area diode and other lamps, which are increasingly used for annealing to release residual stress in LPBF [71,72], holds significant potential for industry applications.

In this paper, the in-situ lock-in thermography is employed to measure the thermal diffusivity and thickness of stainless-steel 304 L powder inside a commercial LPBF machine. To simplify the experimental setup, the LPBF laser is diffused through an optical diffuser, serving as the active heat source. The diffused laser illumination is modulated to provide square thermal wave heating, while a LWIR camera captures the

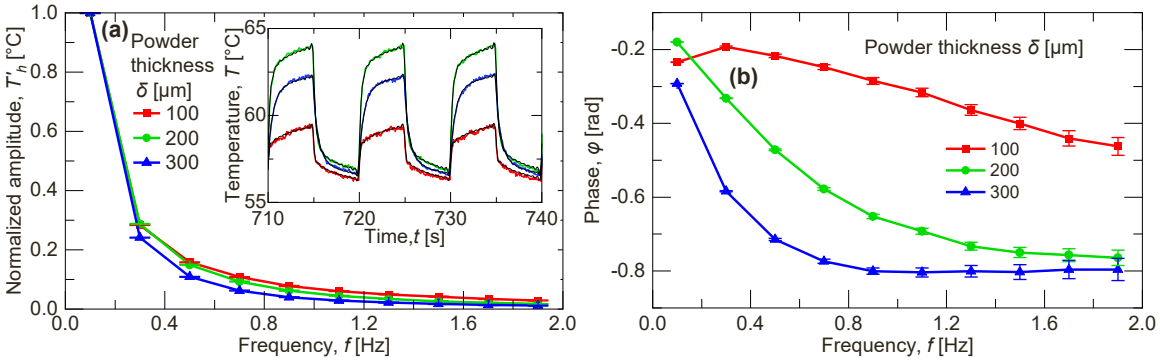

Fig. 2. The experimental (a) amplitude $T_{h,i}$ and (b) phase φ_i of different powder thicknesses in the frequency domain. The inset shows the experimental temperatures along with their corresponding fitting curves.

temperature history of the powder surface. The frequency domain response, including phase and amplitude, of the temperature history is extracted using the least square fitting method. These results are then compared to a 1D thermal transport model, which predicts the phases difference as functions of thermal diffusivity and layer thickness. By fitting the model results to the experiment, the thermal diffusivity of the powder layer is estimated, allowing for the quantification of the effects of powder particle size and wiper spreading speed on the powder's thermal diffusivity. It is also employed to effectively measure the powder layer thickness over printed geometries in a short time. These findings suggest that the lock-in thermographic technique has the potential to provide rapid in-situ inspection of the powder layer in LPBF, enabling real-time detection of anomalies or deviations in product quality.

2. Experimental setup and frequency response extraction

2.1. Experiment setup

Fig. 1(a) illustrates the experimental setup featuring a LWIR camera (FLIR A655sc) integrated with a commercial LPBF system (Renishaw AM250). This LPBF uses a fiber laser (SPI R4 RedPOWER, UK) with a maximum power of 200 W, wavelength of 1070 μm, and spot diameter of 75 μm. A ZnSe window was installed on the chamber ceiling. This enables a LWIR camera to observe the build plate from a 15° off-normal angle outside of the chamber. After reducing the region of interest to 640 × 120 pixels the camera records images at 200 frames per second, and its Nyquist limit (100 Hz) is much higher than the highest applied thermal wave frequency in this paper. The equivalent pixel size on the build plate is 325 μm/pixel for this configuration with a noise equivalent temperature difference (NEDT) of 30 mK reported by the camera vendor. Assuming a gray body emissivity of 0.95 for the testing, the frequency-domain approach prioritizes the linear variation of the measured temperature rather than the exact temperature value.

After the parts are deposited using the LPBF process, a 100 × 100 mm^2 square optical diffuser (DG100×100–220, Thorlabs) is swung into the beam path for the LPBF laser. The optical diffuser is 30 cm above the powder bed and spreads the LPBF laser to illuminate an area around 10 cm diameter on the powder bed surface (See Fig. 1(b)). During the thermographic inspection process, the LPBF scan head is commanded to switch between building part A in the center of the build plate (transmits the optical diffuser) and part B at the corner (bypasses the optical diffuser). This generates a square thermal wave intensity modulation in part A area, discussed in more detail in Appendix A. This strategy allows the frequency of the square thermal wave to be adjusted as well as its duty cycle (50 % for the experiments presented in this paper). The thermal wave illumination from the diffused LPBF laser beam heats the powder bed. The temperature response of the powder is a function of both the powder layer thickness and its thermal properties.

To control the powder layer thickness, immediately prior to the experiment, seven rectangular blocks (10 ×10 mm^2) with varying heights h_i were printed. 304 L stainless steel powder (Carpenter Technology, USA) with a particle diameter of 15 – 45 μm is utilized in this paper, unless otherwise noted. When the wiper spreads a fresh layer of powder at datum, h_0, the local thickness of the powder layer is given by $\delta_i = h_0 - h_i$. This ranges from 50 to 350 μm in 50 μm increments. Fig. 1(c) displays the measured temperature history for the 78 cycles at the part A region of three blocks, corresponding to powder layer thicknesses of 100, 200 and 300 μm. The last several cycles are magnified in Fig. 1(d). In each cycle, the temperature rises when the diffuse laser beam illuminates part A before cooling during the part B illumination of the cycle. The figures show that the temperature history is the superposition of transient (gradual heating in Fig. 1(c)) and steady-state harmonic response (highlighted periodic heating in Fig. 1(d)). The thermal images at specific times are shown in Fig. 1(e) and (f). The Video S1 in supplementary shows thermal history imaging. As would be expected, the diffusion of the laser by the optical diffuser leads to variance in the amplitude of the temperature rise as a non-uniform distribution (Fig. 1(f)). Working in the frequency domain avoids this being an issue.

Supplementary material related to this article can be found online at doi:10.1016/j.addma.2023.103726.

In an ideal scenario, the utilization of multiple individual sinusoidal thermal waves with controlled frequencies and amplitudes for phase measurement is expected to yield higher accuracy compared to square wave measurements. This is attributed to the fact that the controlled sinusoidal frequency induces a thermal response exclusively at its modulated frequency, thereby reducing the presence of noise. However, the primary objective of this paper is to present the concept of the thermal wave method and demonstrate its feasibility by using a simplified square thermal wave as a special case.

2.2. Frequency response extraction

The square thermal wave of the time dependent laser illumination q_{laser} can be expanded using an infinite Fourier series as,

$$q_{laser} = \frac{I_0}{2} + \sum_{n=1}^{\infty} \frac{2I_0}{n\pi} \, sin(2\pi f_n t) \tag{1}$$

where I_0 is the maximum laser illumination intensity and f_1 is the illumination frequency. Because it is a square wave, some of the energy is distributed to higher order harmonics $f_n = (2n\text{-}1)f_1$, $n = 1, 2, 3\ldots$ A heuristic regression model including an additional phase difference term is used to represent the total temperature response. It can be modeled using a Fourier series-based regression model as:

$$T(t) = T_i(t) + T_h(t) = T_i(t) + \sum_{n=1}^{\infty} T_{h,n} \, sin(2\pi f_n t + \varphi_n) \tag{2}$$

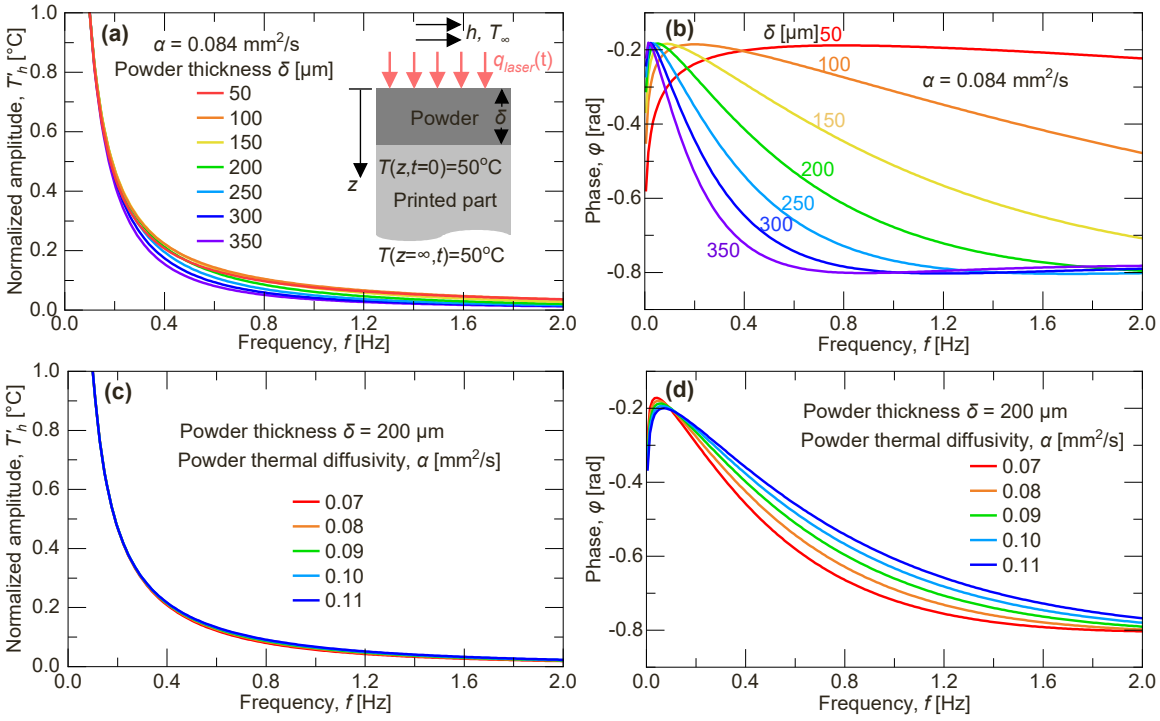

Fig. 3. Frequency domain finite difference solution of the 1D heat diffusion model, (a) amplitude and (b) phase as a function of powder thickness, and (c) amplitude and (d) phase as a function of powder thermal diffusivity.

where T_t is the time dependent transient portion of the response, which is related to the step response of the applied $I_0/2$ input term in Eq.(1), $T_{h,n}$ is the amplitude of the harmonic response, T_h, at frequency f_n, and φ_n is the phase lag between the response temperature and illumination thermal wave q_{laser} at frequency f_n. These parameters can be extracted by applying a linear least square fitting to Eq. (2) in order to accurately match the experimental temperature response. The transient portion of the response can be fit using a polynomial of powers of t and $t^{1/2}$ while values of $T_{h,n}$ and phase φ_n, which do not vary with t, can be fit after the following modification:

$$T_t(t) = A_1 + A_2\sqrt{t} + A_3 t$$
$$T_h(t) = \sum_{n=1}^{\infty} T_{h,n} sin(2\pi f_n t + \varphi_n) = \sum_{n=1}^{\infty} [G_n sin(2\pi f_n t) + H_n cos(2\pi f_n t)\,] \quad (3)$$

where the coefficients A_1, A_2, A_3, G_n and H_n can be fit directly and G_n and H_n can be converted to $T_{h,n}$ and φ_n with

$$T_{h,n} = \sqrt{G_n^2 + H_n^2}$$
$$\varphi_n = tan^{-1}\left(\frac{H_n}{G_n}\right). \quad (4)$$

The uncertainty analysis for extracting $T_{h,n}$ and φ_n from least square fitting is reported in Appendix B1. In general, the least squares approach is more robust with respect to dropped frames than a direct Fourier transform.

Fig. 2 shows the extracted amplitude $T_{h,n}$ and phase φ_n from the temperature history in Fig. 1(c). The maximum frequency order is $n = 20$. To remove the effects of non-uniform illumination, the amplitude is normalized by $T'_{h,n} = T_{h,n}/T_{h,1}$, where $T_{h,1}$ represents the amplitude at the illumination frequency f_1. Fig. 2 shows that both the amplitude and phase are dependent on the powder layer thickness, with the phase displaying greater sensitivity than the normalized amplitude.

3. 1D heat transport model and finite difference solution

With the square thermal wave illumination, the harmonic steady state diffusion through the powder layer can be modeled using a 1D analysis. This is valid in the center of the printed parts, when the distance from the edge is significantly greater than the powder layer thickness, and assuming that both the powder layer and printed parts behave has a homogeneous effective medium with constant properties (the temperature varies over a small range during the inspection step). The model is illustrated in the inset of Fig. 3(a). In this model, a powder layer of thickness δ is in contact with a printed block. The square thermal wave illumination heat flux $q_{laser}(t)$ is incident onto the top surface of the powder. The absolute value of the laser absorption in the powder is not important due to the normalization of the amplitude but could be extracted if desired. However, the laser interaction is assumed to serve as a heat flux at the exposed surface of the part rather than a volumetric absorption in the powder layer. A convection boundary condition is applied to the exposed surface with $h = 15$ W/m^2·K, to account for the low argon flow over the surface. The ambient temperature is taken as $T_\infty = 30$ °C while the printed block is assumed to be in perfect contact with the build plate, to maintain a constant temperature of $T_{z=\infty} = 50$ °C. Given these constraints, the temperature history of the powder/part system is described by

$$\frac{\partial T}{\partial t} = \alpha_i \frac{\partial^2 T}{\partial z^2} \quad (5)$$

where the i subscript on the thermal diffusivity, α, denotes whether the properties of powder or solid material are used to describe the material locally. This is subject to boundary conditions

$$\alpha_p \left.\frac{\partial T}{\partial z}\right|_{z=0} = \frac{h}{\rho_p c_p}[T(z=0,t) - T_\infty] - \frac{q_{laser}}{\rho_p c_p}$$
$$T_\infty = 30^\circ C \quad (6)$$
$$T(z=\infty, t) = 50^\circ C$$

Table 1
Parameter value for 1D heat transport model [41].

Parameters	304 L Solid	304 L Powder
Density, ρ [kg/m^3]	8030	4352
Specific heat capacity, c [J/kg·K]	490	490
Thermal conductivity, k [Wm/K]	16.2	0.181
Thermal diffusivity, α [mm^2/s]	4.12	0.084

and the initial condition

$$T(z, t = 0) = 50^{\circ}C \tag{7}$$

where T is the temperature, t is the time, and α_p, ρ_p and c_p are the thermal diffusivity, density and the specific heat of powder material. The material values are listed in Table 1.

The thermal wavelength in material is $\lambda = 2\sqrt{\alpha\pi/f}$ [73]. The thermal penetration depth is $\mu = \sqrt{\alpha/\pi f} = \lambda/2\pi$ [74], which describes the characteristic length at which the harmonic part of the temperature field falls to $1/e$ of its value at the source. In general, there is a tradeoff between the print part spatial resolution of the thermal response and its thermal wavelength λ or depth of penetration μ. For example, the longer wavelength λ leads to the blurring temperature distribution on the print part edges, however, the resulting deeper thermal penetration depth μ facilitates the propagation of thermal wave. In this paper, the height of the parts above the build plate is significantly greater than μ and the effects of the build plate on the T_h become negligible for frequencies larger than 0.1 Hz. This allows the problem in Eqs. (5)–(7) to be effectively modeled as semi-infinite in the z direction using a 1D frequency domain finite difference algorithm (detailed in Appendix C). Working in the frequency domain allows solving for the harmonic response at the surface significantly faster than extracting the response from a transient solution. Fig. 3 shows how the amplitude $T_{h,n}$ and phase φ_n vary with powder thicknesses and thermal diffusivity as determined through calculations using a 1D model in frequency domain. It denotes that the normalized amplitude is less sensitive than phase to the variations in the thermal properties of the powder. Consequently, only the phase is used to estimate the powder properties in the subsequent sections of this paper.

4. Lock-in thermographic measurement validation

Fig. 4(a) shows a photograph of the simple gauge specimens described in Section 2, after the powder has been removed, while Fig. 4 (b) shows the blocks inside the LPBF machine after coating fresh powder. The powder thickness is measured using a laser scanning (LMI Gocater 2320). The measured surface heights of the gauge specimens with and without powder are compared to obtain the height of the powder layer which is shown in Fig. 4(c). The specimens were fabricated so that the thickness ranges from 50 to 350 μm on increments of 50 μm.

During the thermal wave experiments, the laser diffusely illuminates the powder bed with 200 W of power. The intensity of the laser is square wave modulated at a frequency of $f_1 = 0.1$ Hz using the scanning strategy in Fig. 1(a) and (b). The temperature of the top surface is recorded by the LWIR camera in the time domain and the amplitude and phase are extracted as discussed in Section 2. Fig. 5(a) and Video S2 in supplementary show 2D phase maps extracted at different harmonic frequencies, f_n. The phase maps for higher harmonics generally appear sharper due to the shorter thermal penetration depth μ. However, the lower amplitude of the thermal response at higher harmonic frequencies also results in a reduced signal to noise value. Fig. 5(b) shows a comparison between the extracted phases (averaged over the blocks) and the 1D thermal transport model. The error bars in this figure indicate the ± one standard deviation about the average value for phases. As shown in the figure, the 1D model phases agree well with the experiment, when the correct thermal properties are selected.

Supplementary material related to this article can be found online at doi:10.1016/j.addma.2023.103726.

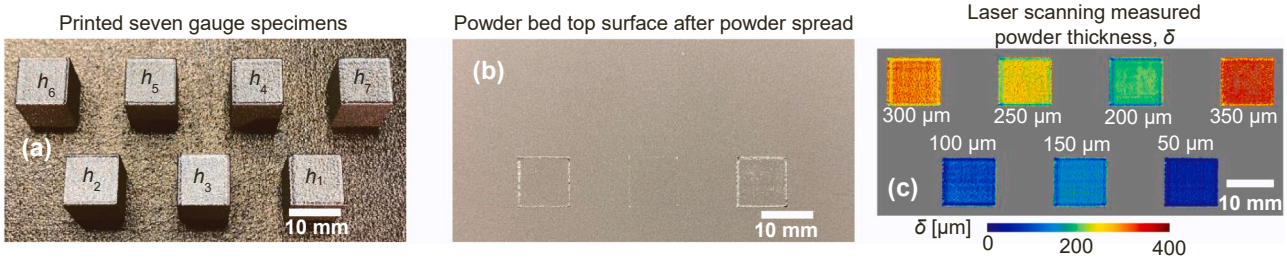

Fig. 4. (a)Photograph of gauge specimens and (b) in-situ powder bed top surface after powder spread, and (c) 2D map of laser scanning measured powder layer thickness.

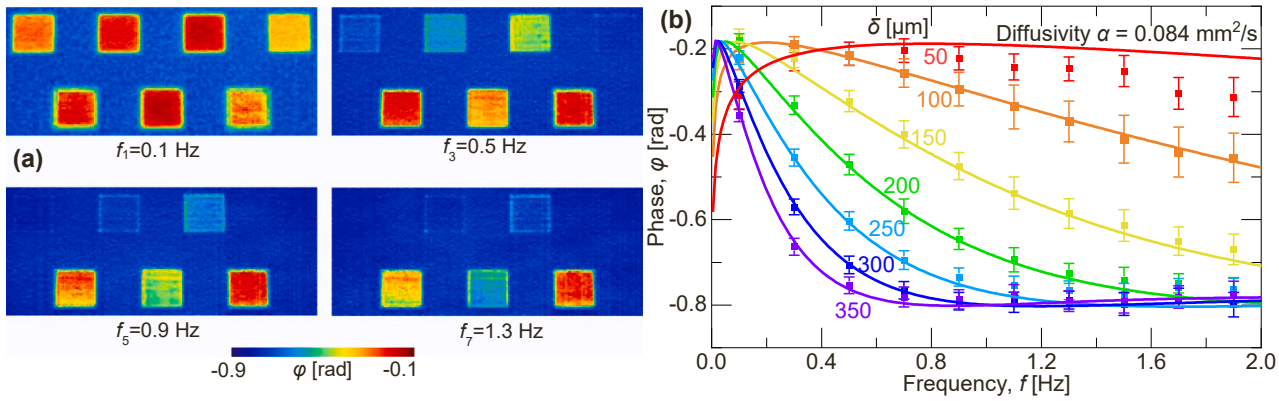

Fig. 5. (a) Phase distribution at different frequencies obtained through least square fitting, and (b) comparison of experimentally extracted phases and 1D model phases.

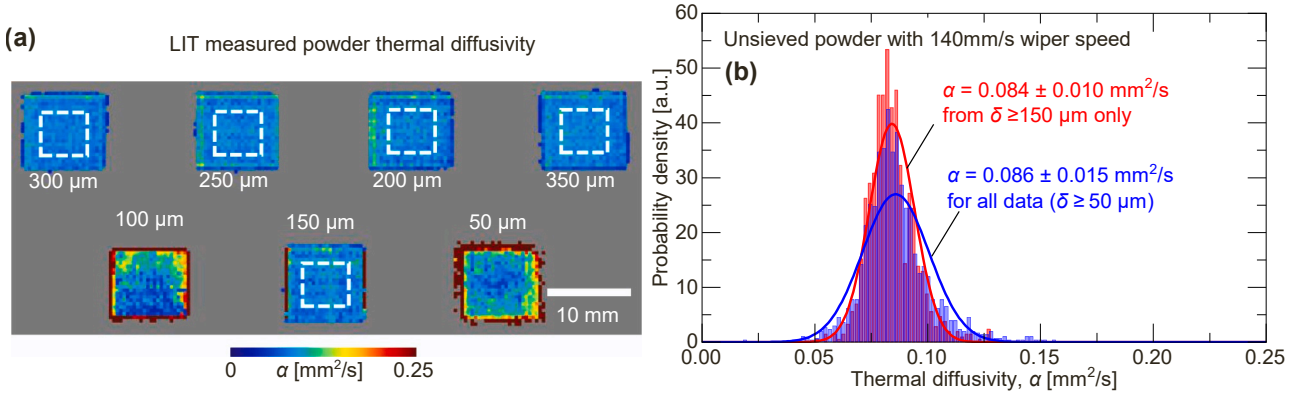

Fig. 6. (a) 2D map of lock-in thermography (LIT) measured thermal diffusivity (white dash line marks the inner area). (b) Thermal diffusivity with normal distribution. The blue curve represents all thickness ($\delta \geq 50$ μm), while the red curve corresponds to the block with higher powder thickness ($\delta \geq 150$ μm).

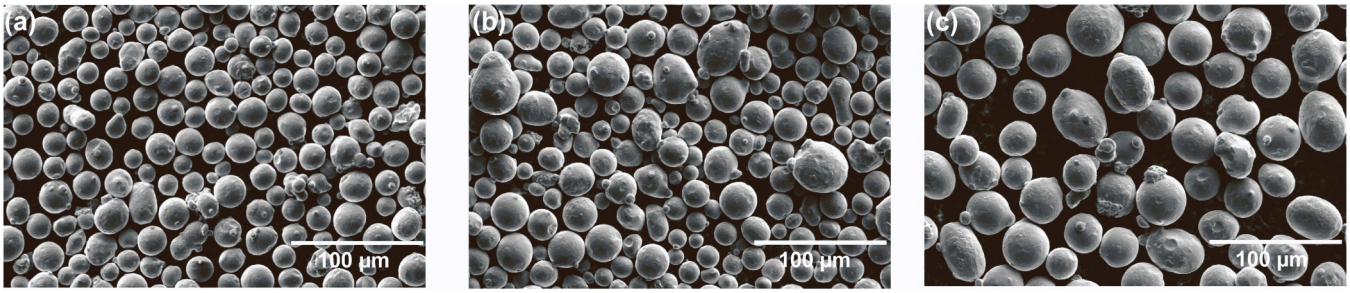

Fig. 7. SEM images of representative samples showing (a) fine, 15 – 25 μm, (b) unsieved as received 15 – 45 μm and (c) coarse powder, 25 – 45 μm powders.

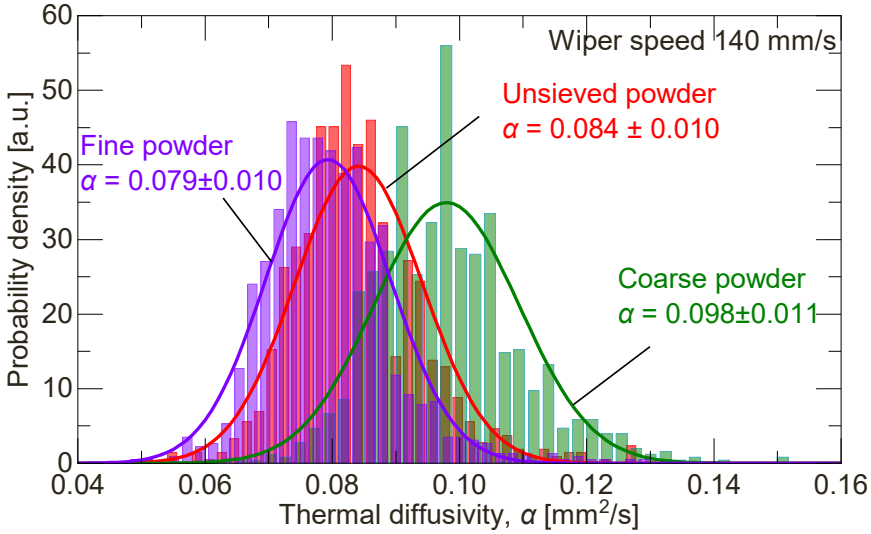

Fig. 8. Thermal diffusivity measurement for different sized powders using lock-in thermography.

The least square method is used to estimate the powder thermal diffusivity α by minimizing the sum of squared errors RSS_φ of the 1D model phases and experimental phases as

$$min(RSS_\varphi) = min\left\{\sum_{n=1}^{N}[\varphi_n - \varphi'(f_n, \alpha, \delta)]^2\right\} \quad (8)$$

where $\varphi'(f_n, \alpha, \delta)$ represents the 1D model calculated phase for thermal diffusivity α and powder layer thickness δ at harmonic frequency f_n, and N is the maximum order of harmonic frequency used in parameter estimation. The first five phase values $\varphi_1 \ldots \varphi_5$ are employed to estimate the powder thermal diffusivity.

Fig. 6(a) shows the 2D map of thermal diffusivity, (with uncertainty analysis in Appendix B2). At the edges of the 50 and 100 μm thick areas, the extracted thermal diffusivity is anomalously high. This is because the spreading powder did not completely cover the edges (see Fig. 4(b)) leading to an effective media comprising of some of the underlying printed part. In the inner area of the 50 and 100 μm thick sections, the thermal diffusivity is lower. This may be caused by increased voids from particle jamming [30,75]. These voids break the homogeneous effective medium and surface laser interaction assumptions.

Fig. 6(b) shows two histograms of the thermal diffusivity calculated

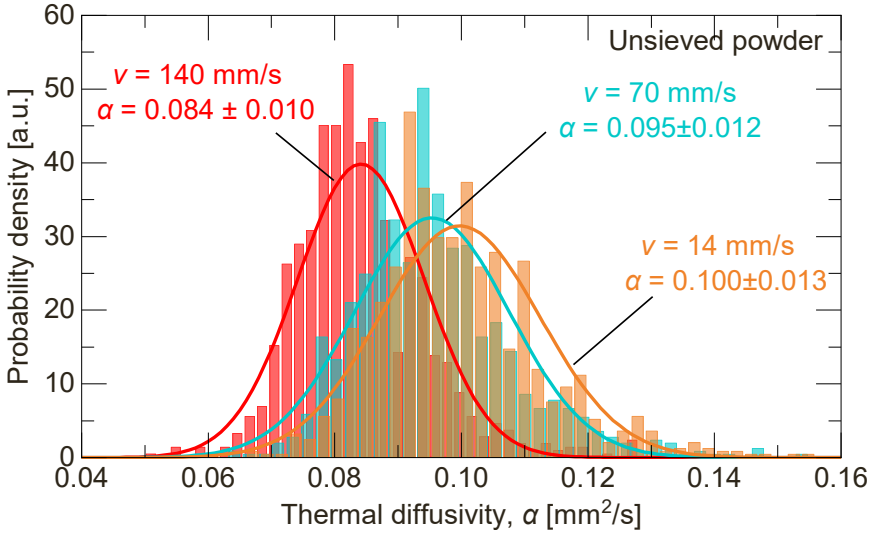

Fig. 9. Thermal diffusivity measurement for different wiper speeds using lock-in thermography.

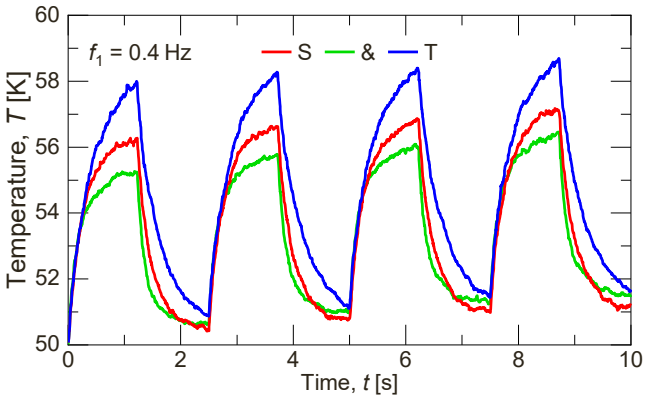

Fig. 10. LWIR camera measured temperature history for selected points at the parts of 'S', '&', and 'T'.

pixel by pixel from the inner area of the blocks. A 95 % confidence interval for the powder thermal diffusivity is calculated by fitting a Gaussian distribution to the histograms. The histogram generated by excluding the 50 and 100 μm (including the nominal powder thicknesses $\delta \geq 150$ μm) is narrower than one created from all seven areas, showing that higher thicknesses ($\delta \geq 150$ μm) produce lower thermal diffusivity uncertainty. As a result, these five blocks ($\delta \geq 150$ μm) are selected for the following section measurements. However, it should be noted that even though the diffusivity measurements are less accurate for layer thicknesses approaching the maximum particle diameter, anomalies in the layers can still be detected.

5. In-situ lock-in thermographic monitoring powder bed for influence of powder size and wiper speed

The lock-in thermographic approach offers a novel tool in LPBF for studying the in-situ thermal diffusivity of the powder layer. Various experimental variables, such as powder particle size and wiper spreading speed, can influence the properties of the powder layer. Accurately characterizing these properties is crucial for modeling efforts as well as monitoring of the process, ensuring the detection of any unintended alterations in the powder layer.

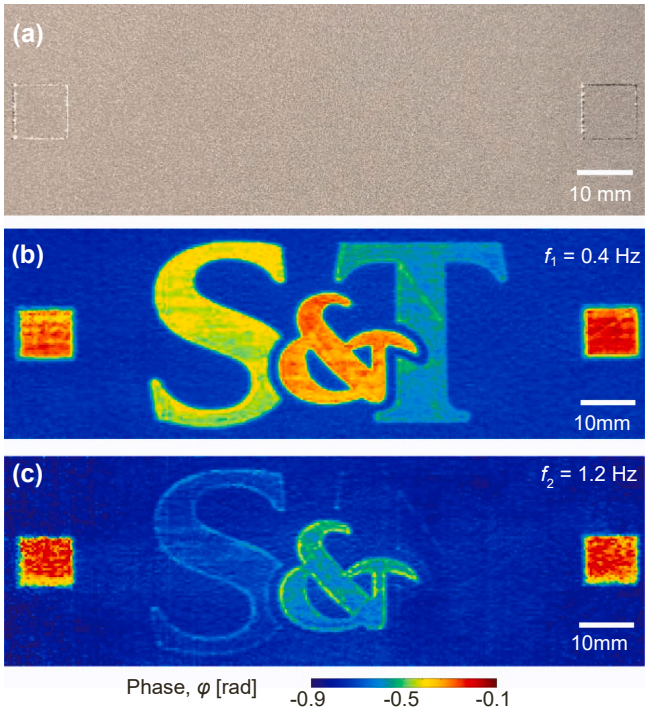

Fig. 11. (a) Photograph of in-situ powder bed top surface after powder spread, and phase maps at (b) 0.4 Hz and (c) 1.2 Hz.

5.1. Powder size

The commercial 304 L stainless steel powder used in this paper has a particle diameter of 15 – 45 μm. To study how the powder size distribution affects the thermal transport properties, the powder was sieved to separate the raw powder into a fine powder distribution (<25 μm) and a coarse powder distribution (>25 μm). Fig. 7 shows the SEM images of the three powder distributions.

The sieved powder is spread individually over printed gauge blocks (shown in Fig. 4(a)). A spreader speed of 140 mm/s is used for all the distributions. After spreading, the same procedure as in Section 4 was used to integrate the powder and fit the thermal diffusivity pixel-by-pixel. Fig. 8 shows histograms of the measured thermal diffusivities

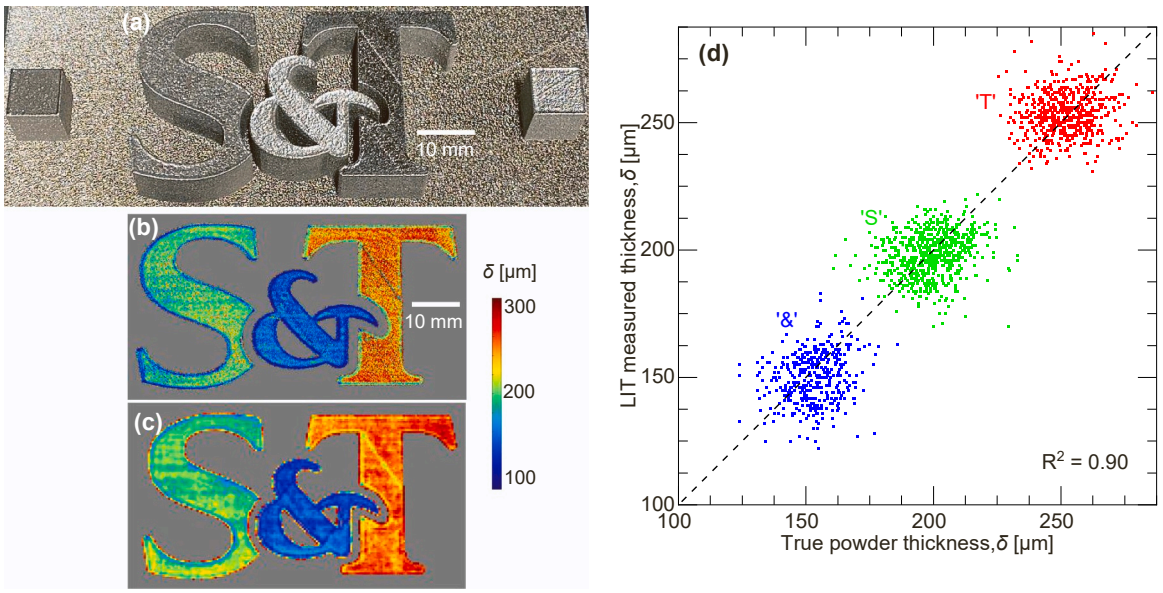

Fig. 12. (a) Photograph of S&T logo after powder bed has been cleaned, (b) true powder thickness from laser scanning, (c) lock-in thermography measured powder thickness, (d) comparison of true powder thicknesses with lock-in thermography measured thickness.

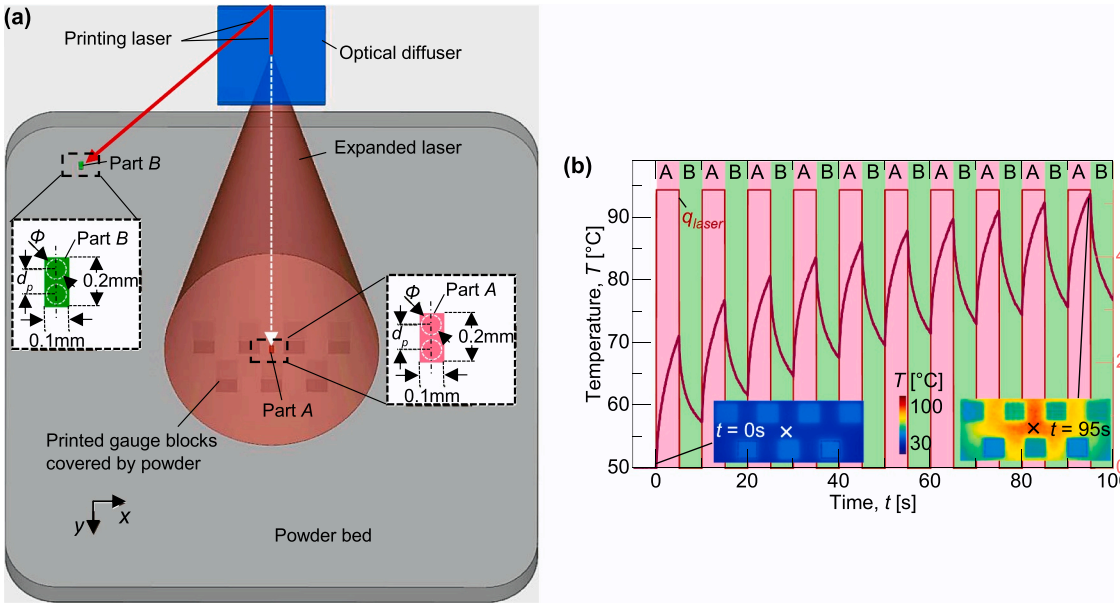

Fig. A1. (a) Schematic of the experimental setup for modulated square wave in Renishaw AM250. (b) Experimentally recorded temperature history captured by LWIR thermal camera.

for the three distributions. The results show that thermal diffusivity increases with particle size in agreement with literature [41]. In general, larger particles have fewer gas interfaces per volume, resulting in reduced thermal resistance and higher thermal conductivity.

5.2. Spreader speed

The commercial LPBF machine allows wiper spreading speeds between 14 and 140 mm/s. With the exception of the experiments in this section, all the experiments in this paper are performed using a spreader speed of 140 mm/s. To understand the effects of spreader speed, the gauge block experiment was repeated with two additional wiper speeds (14 and 70 mm/s) using unseived powder. Fig. 9 shows the fitted pixel-by-pixel thermal diffusivity using the lock-in thermography. The results show that slower wiper speeds lead to an increased thermal diffusivity. This can be attributed to the impact of wiper spreading speeds on porosity, as slower spreading speeds are associated with lower powder bed layer porosity. Porosity affects both the effective density and thermal conductivity. In general, while the density increases with decreasing porosity, thermal conductivity rises much more rapidly when porosity diminishes [76] This increases thermal diffusivity as porosity decreases. These results agree with numerical simulations in literature [28,30,67,75] and suggest that the powder bed density can be monitored using the thermal diffusivity.

6. In-situ lock-in thermographic monitoring for powder layer thickness

The previous sections introduced the lock-in thermography technique. While this can be used for fundamental property measurements, it

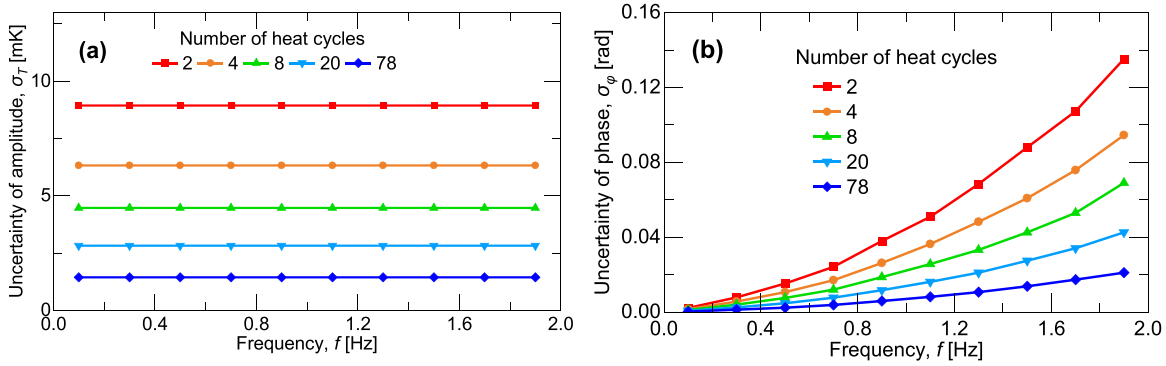

Fig. B1. (a)Uncertainty $\sigma_{Th,n}$ of amplitude $T_{h,n}$ and (b) phase uncertainty $\sigma_{\varphi n}$ for different heat cycles with 200 μm powder layer thickness.

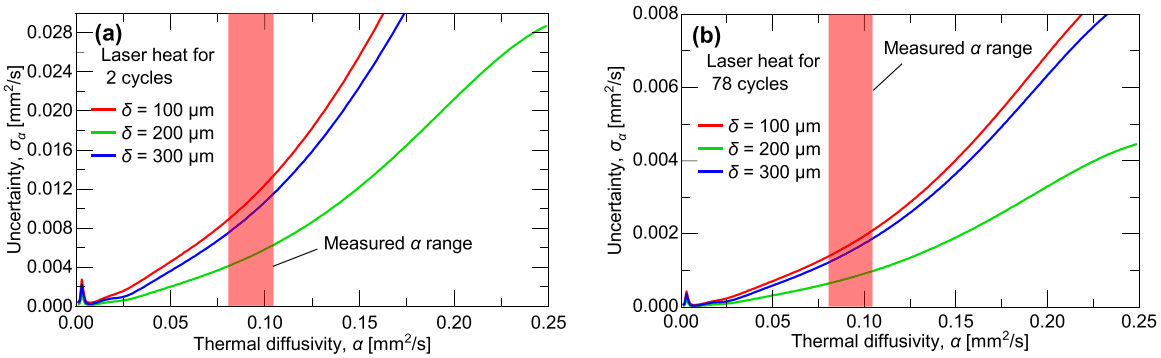

Fig. B2. Uncertainty of thermal diffusivity σ_α for various powder thickness with (a) 2 laser heat cycles and (b) 77 laser heat cycles. The red region represent the measured thermal diffusivity, as detailed in Sections 4 and 5.

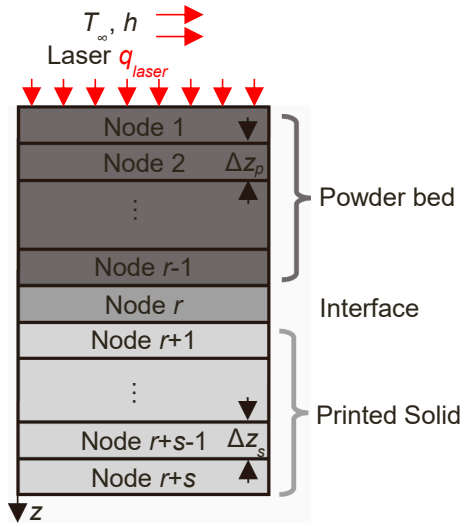

Fig. C1. Schematic of discrete node distribution for 1D heat transfer model.

also has the potential for in-process inspection. Compared with our previous work of passive thermography [63], this section demonstrates the ability of active thermographic method to resolve the thickness using data from a shorter interrogation time (10 s total). Unsieved powder, spread at 140 mm/s is used for this. A university logo "S&T" was created using LPBF with each letter printed to a different height. Specifically, the 'S' symbol has a height 50 μm lower than the '&', and 50 μm higher than the 'T' symbol. The heights of these symbols above the build plate are significantly greater than the thermal penetration depth μ to satisfy the 1D assumption. After printing the highest '&' symbol, the elevator was then lowered by 150 μm and a fresh layer of powder was spread over the part. The 'S', '&', and 'T' symbols are now covered by nominal powder thicknesses of 200 μm, 150 μm, and 250 μm, respectively. The spread powder is then illuminated by the diffused LPBF laser beam. The laser is modulated at $f_1 = 0.4$ Hz and for 4 cycles. Fig. 10 shows the LWIR camera measured temperature history for points inside the three symbols. Fig. 11(a) shows a photograph of the powder coated artifact at this step.

The same procedure as in Section 4 is employed to extract the phase from the recorded temperature history. Fig. 11(b-c) shows the phase maps φ_1 and φ_2 extracted at the first and second harmonic frequencies, $f_1 = 0.4$ Hz and $f_2 = 1.2$ Hz. While the logo cannot be seen in the optical photograph, it becomes clearly discernible in the thermal phase maps. The phase map extracted at the second harmonic ($f_2 = 1.2$ Hz) shows a sharper boundary around the '&' symbol, however, the deeper 'T' cannot be resolved. For this 0.4 Hz illumination frequency, these extract phases φ_1 and φ_2 are utilized for powder thickness measurement. This choice is made because the higher frequency phases ($f_n > f_2$) are heavily influenced by background noise, rendering them less reliable for accurate thickness determination.

Fig. 12(a) shows a photograph of the artifact after removing the powder. The artifact was removed from the build chamber and laser scanned (LMI Gocater 2320) to measure the local powder thickness which is shown Fig. 12(b). Fig. 12(c) shows the estimated powder thickness using Eq. (8) and fitting the 1D model thermal transport model to the measured phases. The powder diffusivity is assumed to be $\alpha = 0.084$ mm^2/s (from Fig. 6). There is good agreement between the ex-situ laser scanning measured powder thicknesses of the artifact and the in-situ thermography extracted powder thickness. This is illustrated by the comparison of the point-by-point thicknesses shown in Fig. 12(d). The coefficient of determination, R^2, for the correlation between the in-situ and ex-situ measured thicknesses, is 0.90. The strong correlation between the measurements even with a reduced integration time (10 s)

suggests that the technique has significant potential for in-process inspection. It is worth noting that the surface topography of artifacts can be deduced from the thickness of the powder layer. For example, there is an elevated region that appears as a linear feature in the middle of the symbol "T" surface (see Fig. 12 (a)). This phenomenon results in a thinner powder layer thickness as shown in the same region in Fig. 12 (c). This surface topography monitoring capability of this method enables the application for real-time detection of anomalies or deviations in LPBF.

7. Conclusion

This paper investigates the use of a lock-in thermographic method to measure local powder layer thermal diffusivity and/or thickness in-situ during the LPBF process. This method generates a thermal wave by modulating a heat source illuminating the powder bed while observing the powder bed's surface temperature using a LWIR camera. Converting the recorded thermal history to the frequency domain allows the phase information to be compared with a 1D model subject to a robust uncertainty analysis. Using this method, the thermal diffusivity of powder with different particle sizes is measured, as well as powder layer at different wiper spreading speeds. This paper also demonstrated the evaluation of the layer thickness in-situ in a short time (10 s). This capability further enhances the application for the in-situ real time diagnostic of product quality and is potentially an alternative to structured light scanning.

While this paper establishes the framework and demonstrates the significant potential of the lock-in thermographic technique, the approach can be improved by (1) using higher dimensional model and including volumetric heating, (2) expanding the fitting to make use of trained machine learning models and (3) improving the heat source with arbitrary temporal thermal topography in order to provide greater control over the frequency content of the excitation. The third technique can either be realized with the LPBF laser and a diffuser or with separate heating sources such as large-area diodes. Regardless, the lock-in thermographic method has significant potential to improve LPBF with increased simultaneous assurance of the powder quality and layer thickness.

CRediT authorship contribution statement

Tao Liu: Conceptualization, Methodology, Investigation, Software, Data Curation, Validation, Formal Analysis, Visualization, Writing – Original Draft, Writing – Review & Editing. **Edward C. Kinzel:** Conceptualization, Methodology, Supervision, Writing – Review & Editing. **Ming C. Leu:** Conceptualization, Methodology, Supervision, Writing – Review & Editing.

Declaration of Competing Interest

The authors declare that they have no known competing financial interests or personal relationships that could have appeared to influence the work reported in this paper.

Data Availability

The data that has been used is confidential.

Acknowledgment

This research work was supported by the Intelligent Systems Center (ISC) at the Missouri University of Science and Technology, USA.

Appendix A. Generation of square thermal wave with the diffused LPBF laser

Lock-in thermographic measurement typically comprises two components: a modulated thermal wave heat source and an infrared camera. In this study, the LPBF laser expanded by an optical diffuser serves as the modulated heating source. The modulated square thermal wave is generated by printing the designed parts using specific scanning strategies. Fig. A1(a) displays the schematic of the modulated square wave setup.

Two rectangular print parts, A and B, are designed with dimensions of 0.2 mm length, 0.1 mm width and 1 mm height. Part B is positioned at the top left, while part A is placed in the center of the build plane. The laser prints part B first, followed by printing part A in sequence. The laser has a Gaussian distribution and diameter of $\Phi \approx 75$ μm. The optical diffuser is mounted at the center of chamber and 30 cm above the build plane. When part A is printed, the laser transmits through the optical diffuser and expands into a large cone shape to illuminate the powder bed center. When part B is printed, the laser bypasses the optical diffuser without illuminating the powder bed center. In the build preparation software, Materialise Magic, part A and B are combined as an integrated part using the Boolean operation. Subsequently, the integrated part is replicated to create 78 identical parts, all overlapping at the same location. With this setup, the laser prints every integrated part one by one, and in each integrated part it follows the aforementioned sequency of printing part B first and then part A.

The powder at the center area is heated every time the laser printing part A. The scanning strategy, including point distance d_p and exposure time t_e are set up as 0.15 mm and 2.5 s to modulate the illumination frequency. Laser prints part A with two pulses in 5 s and the period of one integrated part printing takes 10 s, resulting in a frequency of 0.1 Hz. These settings effectively modulate the frequency of illumination during the printing process. The recorded temperature of powder bed center is shown in Fig. A1(b). The 50 % duty cycle heating portion is caused by part A printing and cooling portion results from part B printing. With this setup, the amplitude and frequency of the square wave can be easily modulated by adjusting the laser power and exposure time.

Appendix B. Uncertainty analysis

Uncertainty analysis of thermal property characterization in thin films has been conducted using thermoreflectance [77] and photoacoustic methods [78]. Following a similar approach, this section investigates the uncertainty of powder thermal diffusivity α derived from experimental noise. The in-situ lock-in thermographic method introduced in this paper employs a known 1D model to fit experimental phases extracted from the temperature history recorded by LWIR camera. In this fitting, the powder thermal diffusivity α is an unknown parameter being estimated. The uncertainty of α arises from the phase signal uncertainty, which is derived from experimental noise. To analyze these, the uncertainty of phase derived from experimental noise is studied first. Subsequently, the uncertainty of thermal diffusivity caused by phase is derived.

B1. Uncertainty of experimental phase derived from experimental noise

Given the experimental measured phase φ with mean value φ^* and uncertainty σ_φ, this uncertainty σ_φ can be represented as

$$\sigma_{\varphi_n} = \sqrt{\left(\varphi_n - \varphi_n^*\right)^2} \tag{9}$$

where φ_n, $n = 1,2,\ldots N$ are the order n_{th} measured phase data point at frequency f_n. From Eq. (4), the measured experimental phase φ_n is a function of coefficients G_n and H_n as

$$\varphi_n = tan^{-1}[H_n/G_n]. \tag{10}$$

Consider G_n and H_n as the estimated values of G_n and H_n with mean values G_n* and H_n* and uncertainties σ_{Gn} and σ_{Hn}. If φ_n is in a small neighborhood around the mean value φ_n*, φ_n can be expanded around φ_n* with respect to G_n and H_n by the first-order Taylor expansion as

$$\varphi_n \approx \varphi_n^* + \left(G_n - G_n^*\right)\frac{\partial \varphi_n}{\partial G_n} + \left(H_n - H_n^*\right)\frac{\partial \varphi_n}{\partial H_n}. \tag{11}$$

Substituting Eq. (11) into the uncertainty $\sigma_{\varphi n}$, Eq. (9), it can be represented as

$$\sigma_{\varphi_n} = \sqrt{\left[\left(G_n - G_n^*\right)\frac{\partial \varphi_n}{\partial G_n} + \left(H_n - H_n^*\right)\frac{\partial \varphi_n}{\partial H_n}\right]^2} = \sqrt{\left(\sigma_{G_n}\frac{\partial \varphi_n}{\partial G_n}\right)^2 + \left(\sigma_{H_n}\frac{\partial \varphi_n}{\partial H_n}\right)^2 + 2cov(G_n, H_n)\frac{\partial \varphi_n}{\partial G_n}\frac{\partial \varphi_n}{\partial H_n}} = \sqrt{\left(\frac{H_n}{H_n^2 + G_n^2}\sigma_{G_n}\right)^2 + \left(\frac{G_n}{H_n^2 + G_n^2}\sigma_{H_n}\right)^2} \tag{12}$$

where $cov(G_n, H_n)$ is the variance-covariance matrix, defined as $cov(G_n, H_n) = (G_n\text{-}G_n^*)(H_n\text{-}H_n^*)$. Given that G_n and H_n are independent of one another, the variance-covariance matrix $cov(G_n, H_n)$ is equal to zero. The other partial differential terms in Eq. (12) are calculated using Eq. (10). Similarly, the experimentally measured amplitude uncertainty $\sigma_{Th,n}$ is

$$\sigma_{T_{h,n}} = \sqrt{\left(\sigma_{G_n}\frac{\partial T_{h,n}}{\partial G_n}\right)^2 + \left(\sigma_{H_n}\frac{\partial T_{h,n}}{\partial H_n}\right)^2} = \sqrt{\left(\frac{G_n}{\sqrt{H_n^2 + G_n^2}}\sigma_{G_n}\right)^2 + \left(\frac{H_n}{\sqrt{H_n^2 + G_n^2}}\sigma_{H_n}\right)^2}. \tag{13}$$

The uncertainty σ_{Gn} and σ_{Hn} in Eqs. (12) and (13) can be derived from the least square fitting process.

$$RSS_T = \sum_{m=1}^{M}\left[T_m - T_{m,fit}(A_1, A_2, A_3, G_1, H_1 \cdots G_N, H_N)\right]^2 \tag{14}$$

where M denotes the total number of frames in the measured temperature time history, and RSS_T corresponds to the residual sum of squared errors. T_m represents the experimental temperature captured at frame time t_m. $T_{m,fit}$ is the calculated temperature at t_m using

$$T_{m,fit} = A_1 + A_2\sqrt{t_m} + A_3 t_m + \sum_{n=1}^{N}[G_n\, sin(2\pi f_n t_m) + H_n\, cos(2\pi f_n t_m)] \tag{15}$$

When RSS_T reaches its minimum value, it will satisfy:

$$\left.\frac{\partial RSS_T}{\partial A_1}\right|_{\hat{A}_1,\ldots,\hat{H}_N} = 0, \ldots, \left.\frac{\partial RSS_T}{\partial H_N}\right|_{\hat{A}_1,\ldots,\hat{H}_N} = 0. \tag{16}$$

Substituting Eq. (14) into above relationships, it can be obtain that

$$\sum_{m=1}^{M}\left[T_m - T_{m,fit}(\widehat{A}_1, \cdots \widehat{H}_N)\right]\left.\frac{\partial T_{m,fit}}{\partial A_1}\right|_{\hat{A}_1,\cdots\hat{H}_N} = 0, \ldots, \sum_{m=1}^{M}\left[T_m - T_{m,fit}(\widehat{A}_1, \cdots \widehat{H}_N)\right]\left.\frac{\partial T_{m,fit}}{\partial H_N}\right|_{\hat{A}_1,\cdots\hat{H}_N} = 0. \tag{17}$$

By applying a first order Taylor expansion of $T_{m,fit}$ around the mean values G_n* and H_n*, the following results are obtained.

$$T_{m,fit}(\widehat{A}_1, \cdots \widehat{H}_N) \approx T_{m,fit}(A_1^*, \cdots H_N^*) + \left(\widehat{A}_1 - A_1^*\right)\left.\frac{\partial T_{m,fit}}{\partial A_1}\right|_{A_1^*,\cdots H_N^*}, \ldots, + \left(\widehat{H}_N - H_N^*\right)\left.\frac{\partial T_{m,fit}}{\partial H_N}\right|_{A_1^*,\cdots H_N^*} \tag{18}$$

Substituting it into the minimization conditions Eq. (17) and using the approximation

$$\left.\frac{\partial T_{m,fit}}{\partial A_1}\right|_{A_1^*,\cdots H_N^*} \approx \left.\frac{\partial T_{m,fit}}{\partial A_1}\right|_{\hat{A}_1,\cdots\hat{H}_N} \cdots \left.\frac{\partial T_{m,fit}}{\partial H_N}\right|_{A_1^*,\cdots H_N^*} \approx \left.\frac{\partial T_{m,fit}}{\partial H_N}\right|_{\hat{A}_1,\cdots\hat{H}_N} \tag{19}$$

it can be obtained that

$$\begin{aligned}
&\sum_{m=1}^{M}\left[T_m - T_{m,fit}(A_1^*, \cdots H_N^*) - \left(\widehat{A}_1 - A_1^*\right)\left.\frac{\partial T_{m,fit}}{\partial A_1}\right|_{A_1^*,\cdots H_N^*} \cdots - \left(\widehat{H}_N - H_N^*\right)\left.\frac{\partial T_{m,fit}}{\partial H_N}\right|_{A_1^*,\cdots H_N^*}\right]\left.\frac{\partial T_{m,fit}}{\partial A_1}\right|_{A_1^*,\cdots H_N^*} = 0 \\
&\qquad\qquad \vdots \\
&\sum_{m=1}^{M}\left[T_m - T_{m,fit}(A_1^*, \cdots H_N^*) - \left(\widehat{A}_1 - A_1^*\right)\left.\frac{\partial T_{m,fit}}{\partial A_1}\right|_{A_1^*,\cdots H_N^*} \cdots - \left(\widehat{H}_N - H_N^*\right)\left.\frac{\partial T_{m,fit}}{\partial H_N}\right|_{A_1^*,\cdots H_N^*}\right]\left.\frac{\partial T_{m,fit}}{\partial H_N}\right|_{A_1^*,\cdots H_N^*} = 0.
\end{aligned} \tag{20}$$

This relationship can be represented in Matrix form by using Jacobian matrix J

$$J^T\left(\begin{pmatrix} T_1 - T_{1,fit}\left(A_1^*, \cdots H_N^*\right) \\ \vdots \\ T_M - T_{M,fit}\left(A_1^*, \cdots H_N^*\right) \end{pmatrix} - J\begin{pmatrix} \widehat{A}_1 - A_1^* \\ \vdots \\ \widehat{H}_N - H_N^* \end{pmatrix}\right) = \begin{pmatrix} 0 \\ \vdots \\ 0 \end{pmatrix} \tag{21}$$

where Jacobian matrix J is

$$J^T = \begin{pmatrix} \left.\frac{\partial T_{1,fit}}{\partial A_1}\right|_{A_1^*, \cdots H_N^*} & \cdots & \left.\frac{\partial T_{M,fit}}{\partial A_1}\right|_{A_1^*, \cdots H_N^*} \\ \vdots & \ddots & \vdots \\ \left.\frac{\partial T_{1,fit}}{\partial H_N}\right|_{A_1^*, \cdots H_N^*} & \cdots & \left.\frac{\partial T_{M,fit}}{\partial H_N}\right|_{A_1^*, \cdots H_N^*} \end{pmatrix}. \tag{22}$$

When J^TJ is non-singular, Eq. (21) can be rearranged to express the estimate G_n and H_n in terms of G_n*, H_n* and Jacobian matrix J as

$$\begin{pmatrix} \widehat{A}_1 \\ \vdots \\ \widehat{H}_N \end{pmatrix} = \left(J^TJ\right)^{-1}J^T\begin{pmatrix} T_1 - T_{1,fit}\left(A_1^*, \ldots, H_N^*\right) \\ \vdots \\ T_M - T_{M,fit}\left(A_1^*, \ldots, H_N^*\right) \end{pmatrix} + \begin{pmatrix} A_1^* \\ \vdots \\ H_N^* \end{pmatrix}. \tag{23}$$

The standard deviation uncertainty σ_{Gn} and σ_{Hn} of the estimated coefficients G_n and H_n can be obtained from the main diagonal of variance-covariance matrix of coefficients as

$$V\begin{pmatrix} \widehat{A}_1 \\ \vdots \\ \widehat{H}_N \end{pmatrix} = E\left\{\left[\begin{pmatrix} \widehat{A}_1 \\ \vdots \\ \widehat{H}_N \end{pmatrix} - E\begin{pmatrix} \widehat{A}_1 \\ \vdots \\ \widehat{H}_N \end{pmatrix}\right]\left[\begin{pmatrix} \widehat{A}_1 \\ \vdots \\ \widehat{H}_N \end{pmatrix} - E\begin{pmatrix} \widehat{A}_1 \\ \vdots \\ \widehat{H}_N \end{pmatrix}\right]^T\right\} \tag{24}$$

where the expectation value of estimated coefficients G_n and H_n, Eq. (23) is:

$$E\begin{pmatrix} \widehat{A}_1 \\ \vdots \\ \widehat{H}_N \end{pmatrix} = \left(J^TJ\right)^{-1}J^T\begin{pmatrix} E(T_1) - T_{1,fit}\left(A_1^*, \ldots, H_N^*\right) \\ \vdots \\ E(T_M) - T_{M,fit}\left(A_1^*, \ldots, H_N^*\right) \end{pmatrix} + \begin{pmatrix} A_1^* \\ \vdots \\ H_N^* \end{pmatrix}. \tag{25}$$

Substituting Eq. (23) and Eq. (25) into variance-covariance matrix Eq. (24),

$$V\begin{pmatrix} \widehat{A}_1 \\ \vdots \\ \widehat{H}_N \end{pmatrix} = E\left\{\left[\left(J^TJ\right)^{-1}J^T\begin{pmatrix} T_1 - E(T_1) \\ \vdots \\ T_M - E(T_M) \end{pmatrix}\right]\left[\left(J^TJ\right)^{-1}J^T\begin{pmatrix} T_1 - E(T_1) \\ \vdots \\ T_M - E(T_M) \end{pmatrix}\right]^T\right\} \tag{26}$$

and using the matrix property $(AB)^{\mathrm{T}} = B^{\mathrm{T}}A^{\mathrm{T}}$ and $[(J^TJ)^{-1}]^{\mathrm{T}} = (J^TJ)^{-1}$ since $(J^TJ)^{-1}$ is a symmetric matrix, variance-covariance matrix can be simplified as

$$V\begin{pmatrix} \widehat{A}_1 \\ \vdots \\ \widehat{H}_N \end{pmatrix} = \left\{\left(J^TJ\right)^{-1}J^TE\begin{pmatrix} T_1 - E(T_1) \\ \vdots \\ T_M - E(T_M) \end{pmatrix}\begin{pmatrix} T_1 - E(T_1) \\ \vdots \\ T_M - E(T_M) \end{pmatrix}^T J\left(J^TJ\right)^{-1}\right\} = \left(J^TJ\right)^{-1}J^T\begin{pmatrix} \sigma_{T_1}^2 & \cdots & cov(T_1, T_M) \\ \vdots & \ddots & \vdots \\ cov(T_M, T_1) & \cdots & \sigma_{T_M}^2 \end{pmatrix}J\left(J^TJ\right)^{-1}. \tag{27}$$

Assuming that the temperature uncertainty σ_{Tm} is equal for each individual measurement, the σ_{Tm} for powder layer measured by the utilized LWIR camera is determined to be 0.4 K. The standard deviation uncertainties σ_{Gn} and σ_{Hn} of the estimate value G_n and H_n are obtained from the square root of the main diagonal entries in the variance-covariance matrix given by Eq. (27). These uncertainties σ_{Gn} and σ_{Hn} are used to calculate the uncertainties $\sigma_{\varphi n}$ and $\sigma_{Th,n}$ using Eqs. (12) and (13). The uncertainty $\sigma_{Th,n}$ for different laser heating cycles with 200 μm thickness are illustrated in Fig. B1(a). It is evident that the longer heating cycles result in lower uncertainties. Furthermore, the uncertainty $\sigma_{Th,n}$ is independent with frequency, which is attributed to the orthogonal properties of Fourier series obtained from the J^TJ matrix. Fig. B1(b) illustrates the uncertainty of the phase concerning frequency for a 200 μm powder thickness. It is evident that uncertainty increases with higher frequencies, while longer heating cycles help reduce the uncertainty level.

B2. Uncertainties of thermal diffusivity α from least square method.

The thermal diffusivity α is estimated from the least square fitting of 1D model calculated phase $\varphi'(f_n, \alpha, \delta)$ with experimental phase data φ_n by using Eq. (8). Following the same procedures derived in section B1, the variance-covariance matrix of the estimated thermal diffusivity $\widehat{\alpha}$ is:

$$\sigma_\alpha^2 = \left(J^TJ\right)^{-1}J^T\begin{pmatrix} \sigma_{\varphi_1}^2 & \cdots & cov(\varphi_1, \varphi_N) \\ \vdots & \ddots & \vdots \\ cov(\varphi_N, \varphi_1) & \cdots & \sigma_{\varphi_N}^2 \end{pmatrix}J\left(J^TJ\right)^{-1} \tag{28}$$

where Jacobian matrix J in this condition is

$$J = \begin{pmatrix} \left.\dfrac{\partial \varphi_{1D}(f_1,\delta,\alpha)}{\partial \alpha}\right|_{\alpha^*} \\ \vdots \\ \left.\dfrac{\partial \varphi_{1D}(f_N,\delta,\alpha)}{\partial \alpha}\right|_{\alpha^*} \end{pmatrix}. \tag{29}$$

The standard deviation uncertainty σ_α is obtained from the square root of the main diagonal entries in the variance-covariance matrix of Eq. (28). The uncertainty σ_α with different powder thicknesses and laser heat cycles is shown in Fig. B2. The results denote that a 200 μm powder thickness exhibits better accuracy than the other two thickness. It is also demonstrated that with only 2 heating cycles, the uncertainty is around 0.005 mm^2/s. The uncertainty with 78 cycles is around 0.001 mm^2/s, which corresponds to 2.5 % of measured thermal diffusivities shown in Sections 4 and 5.

Appendix C. Solving heat transport equation in frequency domain

To Solve the heat transport equation in frequency domain, it is necessary to eliminate the time terms from the heat transport equation. To achieve this goal, the laser intensity Eq. (1) and temperature response Eq. (2) need to be rewritten with the imaginary part of exponential base functions first,

$$\begin{aligned} q_{laser} &= \frac{I_0}{2} + \sum_{n=1}^{\infty} \mathrm{Im}\left[\frac{2I_0}{n\pi} e^{j2\pi f_n t}\right] \\ T(z,t) &= T_t(z,t) + \sum_{n=1}^{\infty} \mathrm{Im}\left[\tilde{T}_{h,n}(z) e^{j2\pi f_n t}\right] \end{aligned} \tag{30}$$

where $T_{h,n}(z) = T_{h,n}(z)e^{j\varphi_n}$ represents the complex temperature and j is the imaginary unit. By substituting Eq. (30) into the heat equation Eq. (5) and cancel the term $e^{j2\pi f_n t}$, the heat equation can be simplified to

$$\begin{cases} j2\pi f_n \tilde{T}_{h,n}(z) = \alpha \dfrac{\partial^2 \tilde{T}_{h,n}(z)}{\partial z^2} \\ \tilde{T}_{h,n}(z=\infty) = 0 \\ \alpha_p \left.\dfrac{\partial \tilde{T}_{h,n}(z)}{\partial z}\right|_{z=0} = \dfrac{h}{\rho_p c_p} \tilde{T}_{h,n}(z=0) - \dfrac{2I_0}{n\pi\rho_p c_p} \end{cases} \tag{31}$$

which represents the heat equation in the frequency domain with boundary conditions. The finite difference method is employed to numerically solve this heat equation in the frequency domain. Fig. C1 illustrates the discrete node distribution, with node 1 ~ r-1 representing the top powder layer portion and node r + 1 ~ $r + s$ representing the bottom printed solid part portion. Node r corresponds to the interface, while Δz_p and Δz_s denote the node size of powder bed and printed solid, respectively.

The matrix of the finite difference equation is

$$\begin{pmatrix} \Gamma_1 & -1 & & & & & & & \\ 1 & \Gamma_2 & 1 & & & & & & \\ & \ddots & \ddots & \ddots & & & & & \\ & & 1 & \Gamma_{r-1} & 1 & & & & \\ & & & \dfrac{\alpha_p\rho_p c_p}{\Delta z_p} & \Gamma_r & \dfrac{\alpha_s\rho_s c_s}{\Delta z_s} & & & \\ & & & & 1 & \Gamma_{r+1} & 1 & & \\ & & & & & \ddots & \ddots & \ddots & \\ & & & & & & 1 & \Gamma_{r+s-1} & 1 \\ & & & & & & & & 1 \end{pmatrix} \begin{pmatrix} \tilde{T}_{h,n}(1) \\ \tilde{T}_{h,n}(2) \\ \vdots \\ \tilde{T}_{h,n}(r-1) \\ \tilde{T}_{h,n}(r) \\ \tilde{T}_{h,n}(r+1) \\ \vdots \\ \tilde{T}_{h,n}(r+s+1) \\ \tilde{T}_{h,n}(r+s) \end{pmatrix} = \begin{pmatrix} \dfrac{2I_0\Delta z_p}{n\pi\alpha_p\rho_p c_p} \\ 0 \\ \vdots \\ 0 \\ 0 \\ 0 \\ \vdots \\ 0 \\ 0 \end{pmatrix} \tag{32}$$

where

$$\Gamma_m = \begin{cases} \dfrac{\Delta z^2 j\pi f_n}{\alpha_p} + 1 + \dfrac{h\Delta z_p}{\alpha_p\rho_p c_p} & m = 1 \\ -\left(\rho_p c_p \Delta z_p + \rho_s c_s \Delta z_s\right) j\pi f_n - \dfrac{\alpha_p\rho_p c_p}{\Delta z_p} - \dfrac{\alpha_s\rho_s c_s}{\Delta z_s} & m = r \\ -\dfrac{\Delta z^2 j2\pi f_n}{\alpha} - 2 & m = other. \end{cases} \tag{33}$$

The complex temperature $T_{h,n}(z)$ can be solved from this finite difference equation. The modulus and argument of the solution $T_{h,n}(z)$ are the amplitude $T_{h,n}$ and phase φ_n.

References

[1] L. Constantin, N. Kraiem, Z. Wu, B. Cui, J.-L. Battaglia, C. Garnier, J.-F. Silvain, Y. F. Lu, Manufacturing of complex diamond-based composite structures via laser powder-bed fusion, Addit. Manuf. 40 (2021), 101927.

[2] V.Sh Sufiiarov, A.A. Popovich, E.V. Borisov, I.A. Polozov, D.V. Masaylo, A.V. Orlov, The effect of layer thickness at selective laser melting, Procedia Eng. 174 (2017) 126–134.

[3] J.S. Weaver, J. Whiting, V. Tondare, C. Beauchamp, M. Peltz, J. Tarr, T.Q. Phan, M. A. Donmez, The effects of particle size distribution on the rheological properties of the powder and the mechanical properties of additively manufactured 17-4 PH stainless steel, Addit. Manuf. 39 (2021), 101851.

[4] P. Köhnen, S. Ewald, J.H. Schleifenbaum, A. Belyakov, C. Haase, Controlling microstructure and mechanical properties of additively manufactured high-strength steels by tailored solidification, Addit. Manuf. 35 (2020), 101389.

[5] P. Zagade, B.P. Gautham, A. De, T. DebRoy, Analytical estimation of fusion zone dimensions and cooling rates in part scale laser powder bed fusion, Addit. Manuf. 46 (2021), 102222.

[6] X. Tang, X. Chen, F. Sun, L. Li, P. Liu, H. Zhou, S. Fu, A. Li, A study on the mechanical and electrical properties of high-strength CuCrZr alloy fabricated using laser powder bed fusion, J. Alloys Compd. 924 (2022), 166627.

[7] F. Ahsan, J. Razmi, L. Ladani, Experimental measurement of thermal diffusivity, conductivity and specific heat capacity of metallic powders at room and high temperatures, Powder Technol. 374 (2020) 648–657.

[8] H. Gu, C. Wei, L. Li, M. Ryan, R. Setchi, Q. Han, L. Qian, Numerical and experimental study of molten pool behaviour and defect formation in multi-material and functionally graded materials laser powder bed fusion, Adv. Powder Technol. 32 (2021) 4303–4321.

[9] C. Kusuma, S.H. Ahmed, A. Mian, R. Srinivasan, Effect of laser power and scan speed on melt pool characteristics of commercially pure titanium (CP-Ti), J. Mater. Eng. Perform. 26 (2017) 3560–3568.

[10] S. Qu, J. Ding, J. Fu, M. Fu, B. Zhang, X. Song, High-precision laser powder bed fusion processing of pure copper, Addit. Manuf. 48 (2021), 102417.

[11] J. Romano, L. Ladani, J. Razmi, M. Sadowski, Temperature distribution and melt geometry in laser and electron-beam melting processes – a comparison among common materials, Addit. Manuf. 8 (2015) 1–11.

[12] C.S. Lough, T. Liu, X. Wang, B. Brown, R.G. Landers, D.A. Bristow, J.A. Drallmeier, E.C. Kinzel, Local prediction of laser powder bed fusion porosity by short-wave infrared imaging thermal feature porosity probability maps, J. Mater. Process Tech. 302 (2022), 117473.

[13] A. Plotkowski, M.M. Kirka, S.S. Babu, Verification and validation of a rapid heat transfer calculation methodology for transient melt pool solidification conditions in powder bed metal additive manufacturing, Addit. Manuf. 18 (2017) 256–268.

[14] R. Rai, J.W. Elmer, T.A. Palmer, T. DebRoy, Heat transfer and fluid flow during keyhole mode laser welding of tantalum, Ti–6Al–4V, 304L stainless steel and vanadium, J. Phys. D. Appl. Phys. 40 (2007) 5753.

[15] U.S. Bertoli, B.E. MacDonald, J.M. Schoenung, Stability of cellular microstructure in laser powder bed fusion of 316L stainless steel, Mater. Sci. Eng. 739 (2019) 109–117.

[16] Y.M. Ren, Y. Zhang, Y. Ding, T. Liu, C.S. Lough, M.C. Leu, E.C. Kinzel, P. D. Christofides, Finite element modeling of direct metal laser solidification process: sensor data replication and use in defect detection and data reduction via machine learning, Chem. Eng. Res. Des. 171 (2021) 254–267.

[17] L.C. Wei, L.E. Ehrlich, M.J. Powell-Palm, C. Montgomery, J. Beuth, J.A. Malen, Thermal conductivity of metal powders for powder bed additive manufacturing, Addit. Manuf. 21 (2018) 201–208.

[18] T. Craeghs, S. Clijsters, F. Jean.-P. Kruth, Marie-C.Ebert Bechmann, Detection of process failures in layerwise laser melting with optical process monitoring, Phys. Proc. 39 (2012) 753–759.

[19] T. Craeghs, S. Clijsters, E. Yasa, F. Bechmann, S. Berumen, J.-P. Kruth, Determination of geometrical factors in layerwise laser melting using optical process monitoring, Opt. Laser Eng. 49 (2011) 1440–1446.

[20] Y. Kok, X.P. Tan, P. Wang, M.L.S. Nai, N.H. Loh, E. Liu, S.B. Tor, Anisotropy and heterogeneity of microstructure and mechanical properties in metal additive manufacturing: a critical review, Mater. Des. 139 (2018) 565–586.

[21] M. Strantza, R.K. Ganeriwala, B. Clausen, T.Q. Phan, L.E. Levine, D. Pagan, W. E. King, N.E. Hodge, D.W. Brown, Coupled experimental and computational study of residual stresses in additively manufactured Ti-6Al-4V components, Mater. Lett. 231 (2018) 221–224.

[22] C. Qiu, C. Panwisawas, M. Ward, H.C. Basoalto, J.W. Brooks, M.M. Attallah, On the role of melt flow into the surface structure and porosity development during selective laser melting, Acta Mater. 96 (2015) 72–79.

[23] R. Zheng, J. Cui, Y. Yang, S. Li, R.D.K. Misra, K. Kondoh, Q. Zhu, Y. Lu, X. Li, Enhanced densification of copper during laser powder bed fusion through powder surface alloying, J. Mater. Process Tech. 305 (2022), 117575.

[24] U. Ali, Y. Mahmoodkhani, S.I. Shahabad, R. Esmaeilizadeh, F. Liravi, E. Sheydaeian, K.Y. Huang, E. Marzbanrad, M. Vlasea, E. Toyserkani, On the measurement of relative powder-bed compaction density in powder-bed additive manufacturing processes, Mater. Des. 155 (2018) 495–501.

[25] E.J.R. Parteli, T. Pöschel, Particle-based simulation of powder application in additive manufacturing, Powder Technol. 288 (2016) 96–102.

[26] Y. He, A. Hassanpour, A.E. Bayly, Linking particle properties to layer characteristics: Discrete element modelling of cohesive fine powder spreading in additive manufacturing, Addit. Manuf. 36 (2020), 101685.

[27] A.L. Maximenko, I.D. Olumor, A.P. Maidaniuk, E.A. Olevsky, Modeling of effect of powder spreading on green body dimensional accuracy in additive manufacturing by binder jetting, Powder Technol. 385 (2021) 60–68.

[28] L. Cao, Study on the numerical simulation of laying powder for the selective laser melting process, Int. J. Adv. Manuf. Technol. 105 (2019) 2253–2269.

[29] P. Fischer, V. Romano, H.P. Weber, N.P. Karapatis, E. Boillat, R. Glardon, Sintering of commercially pure titanium powder with a Nd:YAG laser source, Acta Mater. 51 (2003) 1651–1662.

[30] J. Zhang, Y. Tan, T. Bao, Y. Xu, X. Xiao, S. Jiang, Discrete element simulation of the effect of roller-spreading parameters on powder-bed density in additive manufacturing, Materials 13 (2020) 2285.

[31] W. Nan, M. Pasha, T. Bonakdar, A. Lopez, U. Zafar, S. Nadimi, M. Ghadiri, Jamming during particle spreading in additive manufacturing, Powder Technol. 338 (2018) 253–262.

[32] S. Haeri, Y. Wang, O. Ghita, J. Sun, Discrete element simulation and experimental study of powder spreading process in additive manufacturing, Powder Technol. 306 (2017) 45–54.

[33] L. Cordova, Z. Chen, Impact of powder recoating speed on built properties in PBF-LB process, Proc. Crip 115 (2022) 125–129.

[34] T. Mukherjee, T. DebRoy, Control of asymmetric track geometry in printed parts of stainless steels, nickel, titanium and aluminum alloys, Comp. Mater. Sci. 182 (2020), 109791.

[35] A. Simchi, The role of particle size on the laser sintering of iron powder, Metall. Mater. Trans. B 35 (2004) 937–948.

[36] C. Meier, R. Weissbach, J. Weinberg, W.A. Wall, A.J. Hart, Critical influences of particle size and adhesion on the powder layer uniformity in metal additive manufacturing, J. Mater. Process Tech. 266 (2019) 484–501.

[37] L.I. Escano, N.D. Parab, L. Xiong, Q. Guo, C. Zhao, K. Fezzaa, W. Everhart, T. Sun, L. Chen, Revealing particle-scale powder spreading dynamics in powder-bed-based additive manufacturing process by high-speed x-ray imaging, Sci. Rep. -Uk 8 (2018) 15079.

[38] R.W. Penny, P.M. Praegla, M. Ochsenius, D. Oropeza, R. Weissbach, C. Meier, W. A. Wall, A.J. Hart, Spatial mapping of powder layer density for metal additive manufacturing via transmission X-ray imaging, Addit. Manuf. 46 (2021), 102197.

[39] M. Qu, Q. Guo, L.I. Escano, J. Yuan, S.M.H. Hojjatzadeh, S.J. Clark, K. Fezzaa, T. Sun, L. Chen, Controlling melt flow by nanoparticles to eliminate surface wave induced surface fluctuation, Addit. Manuf. 59 (2022), 103081.

[40] M. Qu, Q. Guo, L.I. Escano, A. Nabaa, K. Fezzaa, L. Chen, Nanoparticle-enabled increase of energy efficiency during laser metal additive manufacturing, Addit. Manuf. 60 (2022), 103242.

[41] M.R. Alkahari, T. Furumoto, T. Ueda, A. Hosokawa, R. Tanaka, M.S.A. Aziz, Thermal conductivity of metal powder and consolidated material fabricated via selective laser melting, Key Eng. Mater. (2012) 523–524, 244–249.

[42] J.S. Weaver, J. Whiting, V. Tondare, C. Beauchamp, M. Peltz, J. Tarr, T.Q. Phan, M. A. Donmez, The effects of particle size distribution on the rheological properties of the powder and the mechanical properties of additively manufactured 17-4 PH stainless steel, Addit. Manuf. 39 (2021), 101851.

[43] P.A. Kuznetsov, I.V. Shakirov, A.S. Zukov, V.V. Bobyr, M.V. Starytsin, Effect of particle size distribution on the structure and mechanical properties in the process of laser powder bed fusion, J. Phys. Conf. Ser. 1758 (2021), 012021.

[44] A.B. Spierings, N. Herres, G. Levy, Influence of the particle size distribution on surface quality and mechanical properties in AM steel parts, Rapid Prototyp. J. 17 (2011) 195–202.

[45] M.A. Spurek, L. Haferkamp, C. Weiss, A.B. Spierings, J.H. Schleifenbaum, K. Wegener, Influence of the particle size distribution of monomodal 316L powder on its flowability and processability in powder bed fusion, Prog. Addit. Manuf. 7 (2022) 533–542.

[46] K. Riener, N. Albrecht, S. Ziegelmeier, R. Ramakrishnan, L. Haferkamp, A. B. Spierings, G.J. Leichtfried, Influence of particle size distribution and morphology on the properties of the powder feedstock as well as of AlSi10Mg parts produced by laser powder bed fusion (LPBF), Addit. Manuf. 34 (2020), 101286.

[47] M.A. Balbaa, A. Ghasemi, E. Fereiduni, M.A. Elbestawi, S.D. Jadhav, J.-P. Kruth, Role of powder particle size on laser powder bed fusion processability of AlSi10mg alloy, Addit. Manuf. 37 (2021), 101630.

[48] P. Bidare, I. Bitharas, R.M. Ward, M.M. Attallah, A.J. Moore, Laser powder bed fusion in high-pressure atmospheres, Int. J. Adv. Manuf. Technol. 99 (2018) 543–555.

[49] C. Pauzon, P. Forêt, E. Hryha, T. Arunprasad, L. Nyborg, Argon-helium mixtures as laser-powder bed fusion atmospheres: towards increased build rate of Ti-6Al-4V, J. Mater. Process Tech. 279 (2020), 116555.

[50] C. Pauzon, T. Mishurova, S. Evsevleev, S.D.-L. Goff, S. Murugesan, G. Bruno, E. Hryha, Residual stresses and porosity in Ti-6Al-4V produced by laser powder bed fusion as a function of process atmosphere and component design, Addit. Manuf. 47 (2021), 102340.

[51] H. Amano, T. Ishimoto, R. Suganuma, K. Aiba, S.-H. Sun, R. Ozasa, T. Nakano, Effect of a helium gas atmosphere on the mechanical properties of Ti-6Al-4V alloy built with laser powder bed fusion: a comparative study with argon gas, Addit. Manuf. 48 (2021), 102444.

[52] R. Andreotta, L. Ladani, W. Brindley, Finite element simulation of laser additive melting and solidification of Inconel 718 with experimentally tested thermal properties, Finite Elem. Anal. Des. 135 (2017) 36–43.

[53] S. Zhang, B. Lane, J. Whiting, K. Chou, On thermal properties of metallic powder in laser powder bed fusion additive manufacturing, J. Manuf. Process 47 (2019) 382–392.

[54] B. Cheng, B. Lane, J. Whiting, K. Chou, A combined experimental-numerical method to evaluate powder thermal properties in laser powder bed fusion, J. Manuf. Sci. Eng. 140 (2018).
[55] Y. Hu, T.S. Fisher, Accurate thermal diffusivity measurements using a modified Ångström's method With Bayesian statistics, J. Heat. Transf. 142 (2020).
[56] R. Shrestha, W. Kim, Evaluation of coating thickness by thermal wave imaging: a comparative study of pulsed and lock-in infrared thermography – part I: simulation, Infrared Phys. Techn 83 (2017) 124–131.
[57] A. Moskovchenko, V. Vavilov, M. Švantner, L. Muzika, Houdková, active IR thermography evaluation of coating thickness by determining apparent thermal effusivity, Materials 13 (2020) 4057.
[58] M. Larciprete, N. Orazi, Y.-S. Gloy, S. Paoloni, C. Sibilia, R.L. Voti, In-plane thermal diffusivity measurements of polyethersulfone woven textiles by infrared thermography, Sens. Basel Switz. 22 (2022) 940.
[59] Y. Hu, M. Abuseada, A. Alghfeli, S. Holdheim, T.S. Fisher, High-temperature thermal diffusivity measurements using a modified Ångström's method with transient infrared thermography, J. Heat. Transf. 144 (2021).
[60] A. Salazar, M. Colom, A. Mendioroz, Laser-spot step-heating thermography to measure the thermal diffusivity of solids, Int. J. Therm. Sci. 170 (2021), 107124.
[61] K. Tomita, M.Y.L. Chew, A review of infrared thermography for delamination detection on infrastructures and buildings, Sens. Basel Switz. 22 (2022) 423.
[62] S. Hwang, Y.-K. An, J.-M. Kim, H. Sohn, Monitoring and instantaneous evaluation of fatigue crack using integrated passive and active laser thermography, Opt. Laser Eng. 119 (2019) 9–17.
[63] T. Liu, C.S. Lough, H. Sehhat, Y.M. Ren, P.D. Christofides, E.C. Kinzel, M.C. Leu, In-situ infrared thermographic inspection for local powder layer thickness measurement in laser powder bed fusion, Addit. Manuf. 55 (2022), 102873.
[64] F. Ciampa, P. Mahmoodi, F. Pinto, M. Meo, Recent advances in active infrared thermography for non-destructive testing of aerospace components, Sens. Basel Switz. 18 (2018) 609.
[65] G. Giorleo, C. Meola, Comparison between pulsed and modulated thermography in glass–epoxy laminates, Ndt & Int. 35 (2002) 287–292.
[66] X. Zhang, J. Saniie, A. Heifetz, Spatial Temporal Denoised Thermal Source Separation in Images of Compact Pulsed Thermography System for Qualification of Additively Manufactured Metals, 2021 Ieee Int Conf Electro Information Technology Eit. 00 (2021) 209–214.
[67] P. Zhu, D. Wu, Y. Wang, Z. Miao, Defect detectability based on square wave lock-in thermography, Appl. Opt. 61 (2022) 6134.
[68] P.W. Nolte, T. Malvisalo, F. Wagner, S. Schweizer, Thermal diffusivity of metals determined by lock-in thermography, Quant. Infr. Therm. J. 14 (1) (2017) 8.
[69] D. Yao, X. An, H. Fu, H. Zhang, X. Yang, Q. Zou, K. Dong, Dynamic investigation on the powder spreading during selective laser melting additive manufacturing, Addit. Manuf. 37 (2021), 101707.
[70] I. Yadroitsev, Ph Bertrand, I. Smurov, Parametric analysis of the selective laser melting process, Appl. Surf. Sci. 253 (2007) 8064–8069.
[71] J.D. Roehling, W.L. Smith, T.T. Roehling, B. Vrancken, G.M. Guss, J.T. McKeown, M.R. Hill, M.J. Matthews, Reducing residual stress by selective large-area diode surface heating during laser powder bed fusion additive manufacturing, Addit. Manuf. 28 (2019) 228–235.
[72] W.L. Smith, J.D. Roehling, M. Strantza, R.K. Ganeriwala, A.S. Ashby, B. Vrancken, B. Clausen, G.M. Guss, D.W. Brown, J.T. McKeown, M.R. Hill, M.J. Matthews, Residual stress analysis of in situ surface layer heating effects on laser powder bed fusion of 316L stainless steel, Addit. Manuf. 47 (2021), 102252.
[73] C. Ibarra-Castanedo, M. Genest, J.M. Piau, S. Guibert, A. Bendada, X.P. Maldague, Active infrared thermography techniques for the nondestructive testing of materials, Ultrasonic and advanced methods for nondestructive testing and material characterization (2007) 325–348.
[74] P. Jiang, X. Qian, R. Yang, Tutorial: Time-domain thermoreflectance (TDTR) for thermal property characterization of bulk and thin film materials, J. Appl. Phys. 124 (2018), 161103.
[75] P. Tan, F. Shen, W.S. Tey, K. Zhou, A numerical study on the packing quality of fibre/polymer composite powder for powder bed fusion additive manufacturing, Virtual Phys. Prototyp. 16 (2021) 1–18.
[76] F. Ternero, L.G. Rosa, P. Urban, J.M. Montes, F.G. Cuevas, Influence of the total porosity on the properties of sintered materials—a review, Met. -Basel 11 (2021) 730.
[77] J. Yang, E. Ziade, A.J. Schmidt, Uncertainty analysis of thermoreflectance measurements, Rev. Sci. Instrum. 87 (2016), 014901.
[78] K. Herrmann, N.W. Pech-May, M. Retsch, Photoacoustic thermal characterization of low thermal diffusivity thin films, Photoacoustics 22 (2021), 100246.